ChemComm

COMMUNICATION

View Article Online
View Journal | View Issue

Cite this: *Chem. Commun.*, 2026, **62**, 4063

Received 1st December 2025,
Accepted 26th January 2026

DOI: 10.1039/d5cc06830d

rsc.li/chemcomm

Rapid synthesis of high-entropy metal sulfides under ambient conditions as efficient catalysts for the urea oxidation reaction

Linwei Jiang,[a] Yee Xuan Seow,[a] Hsien-Yi Hsu,[b] Mark A. Buntine,[a] Hongpeng Jia,*[c] Zongyou Yin*[d] and Guohua Jia*[a]

Avoiding high-temperature synthesis, high-entropy metal sulfide NiCoFeMnRuS synthesized *via* rapid ambient coprecipitation exhibits outstanding urea oxidation performance, achieving 50 mA cm^{-2} at 1.32 V with excellent stability and energy efficiency.

Electrocatalytic water splitting is a promising route for sustainable hydrogen production, but its efficiency is limited by the sluggish oxygen evolution reaction (OER). To circumvent the bottleneck imposed by the OER, tremendous efforts have been devoted to investigating alternative anodic reactions with favorable thermodynamics.[1,2] Among these, the urea oxidation reaction (UOR) has emerged as a particularly attractive approach, owing to its significantly lower theoretical oxidation potential (0.37 V *vs.* RHE) compared to the OER (1.23 V *vs.* RHE), which enables more energy-efficient hydrogen generation.[3–6] Additionally, the UOR enables lower energy consumption and simultaneous wastewater treatment. However, the complex six-electron transfer process in the UOR requires highly active and durable electrocatalysts.[7–9]

In this context, high-entropy metal compounds (HEMCs), consisting of multiple metal cations with distinct electronic structures, have attracted increasing attention.[10–12] These HEMC catalysts leverage entropy-driven effects, enabling enhanced catalytic activity through synergistic interactions, tunable electronic properties, and the intrinsic presence of highly active catalytic sites.[13,14] Such attributes make HEMCs particularly capable of facilitating intricate multi-electron transfer reactions like the UOR. For instance, Fereja *et al.* synthesized a nanostructured high-entropy oxide $(FeNiCoCrCu)_3O_4$ using a MOF-derived method. The optimized catalyst exhibited a large surface area and rich oxygen vacancies, enabling excellent bifunctional electrocatalytic activity for urea oxidation and oxygen evolution, along with long-term stability and fast charge-transfer kinetics under alkaline conditions.[15] Fu *et al.* synthesized high-entropy $(FeMnMoNi)Se_2$ nanoflowers *via* hydrothermal synthesis, ion exchange, and selenization processes. The catalyst featured multi-active sites with optimized d-band centers, enabling efficient bifunctional performance for the HER and UOR with low overpotentials and excellent stability, showcasing the advantages of high-entropy characteristics.[16] However, most HEMCs still require high-temperature or multi-step synthesis routes involving hydrothermal treatment, annealing, or ion-exchange processes, which not only consume significant energy but also limit compositional tunability and large-scale production. High-entropy metal sulfides have abundant active sites, exceptional structural stability, and superior catalytic performance. However, too the best of our knowledge, no work relating to the urea oxidation reaction based on high-entropy metal sulfides (HEMS) has been reported.

To overcome these barriers, we introduce a rapid co-precipitation strategy for the synthesis of NiCoFeMnRuS at room temperature. This approach dramatically simplifies the HEMS synthesis process, reducing the environmental impact and enhancing the sustainability of catalyst production. Compared with other room-temperature methods reported previously, the present co-precipitation strategy enables much faster and more straightforward HEMS synthesis. The resulting NiCoFeMnRuS catalyst exhibits remarkable efficiency for the UOR, which requires 1.32 V *vs.* RHE to achieve the current density of 50 mA cm^{-2}, along with reliable long-term stability. Furthermore, when employed as the anode in a urea electrolyzer, the NiCoFeMnRuS catalyst achieves a current density of 10 mA cm^{-2} at a cell voltage of just 1.38 V. These results highlight room-temperature high-entropy metal sulfides as

[a] *School of Molecular and Life Sciences, Curtin University, Perth, WA 6102, Australia. E-mail: guohua.jia@curtin.edu.au*
[b] *School of Energy and Environment, Department of Materials Science and Engineering, Centre for Functional Photonics (CFP), City University of Hong Kong, Hong Kong, China*
[c] *CAS Center for Excellence in Regional Atmospheric Environment, and Key Laboratory of Urban Pollutant Conversion, Institute of Urban Environment, Chinese Academy, Xiamen 361021, China. E-mail: hpjia@iue.ac.cn*
[d] *Research School of Chemistry, The Australian National University, Canberra, ACT 2601, Australia. E-mail: zongyou.yin@anu.edu.au*

promising candidates for energy-efficient urea oxidation and wastewater treatment.

A typical synthesis of HEMS nanoflakes involves dissolving Na_2S in water under stirring, followed by injecting a mixed-metal chloride solution (Ni, Co, Fe, Mn, Ru). Notably, the reaction takes place entirely under ambient conditions, making the method not only straightforward and efficient but also highly suitable for upscaling synthesis of HEMS materials (Fig. 1a). Movie S1 presents the synthesis of NiCoFeMnRuS to visually illustrate the reaction process. The rapid kinetics of the coprecipitation process allows metal ions with different solubility products (pK_{sp}) to reach supersaturation concurrently, triggering simultaneous nucleation and growth. This approach overcomes the inherent solubility differences among elements, enabling the formation of a uniform solid solution.[17]

Firstly, the crystal structures of the NiCoFeMnRuS nanoflakes were examined using X-ray diffraction (XRD), as shown in Fig. S1. The pattern exhibits broad and weak diffraction peaks, indicative of low crystallinity, which is a typical characteristic of high-entropy materials. X-ray photoelectron spectroscopy (XPS) was carried out to investigate the chemical states and surface composition of the synthesized NiCoFeMnRuS nanoparticles, as shown in Fig. S2. The survey scan confirms the presence of all six metal elements (Ni, Co, Fe, Mn, Ru) along with sulfur, indicating that the target components were successfully incorporated into the high-entropy metal sulfide structure. The high-resolution Ni 2p spectrum (Fig. S2b) displays two prominent peaks at 855.3 eV and 873.1 eV, corresponding to Ni $2p_{3/2}$ and Ni $2p_{1/2}$, respectively, accompanied by evident satellite features at 861.2 eV and 881.9 eV. These binding energy values are indicative of the predominant presence of Ni^{2+} species.[18,19] As shown in Fig. S2c, the Co 2p spectrum displays characteristic peaks at 780.1 eV (Co $2p_{3/2}$) and 796.3 eV (Co $2p_{1/2}$), along with corresponding satellite features at 784.1 eV and 802.6 eV.[12] The Fe 2p spectrum of the HEMS in Fig. S2d exhibits two distinct peaks at 712.4 eV and 722.3 eV, corresponding to the Fe $2p_{3/2}$ and Fe $2p_{1/2}$ spin–orbit components, respectively.[20] In the Mn 2p spectrum (Fig. S2e), the main peaks at 641.5 eV and 653.4 eV correspond to Mn $2p_{3/2}$ and Mn $2p_{1/2}$, respectively. Additionally, a satellite peak associated with Mn $2p_{3/2}$ is identified at 646.1 eV.[21] In Fig. S2f, the XPS spectrum of Ru displays two well-defined peaks at binding energies of 461.9 eV and 484.1 eV, which can be assigned to the Ru $3p_{3/2}$ and Ru $3p_{1/2}$ spin–orbit components, respectively. The S 2p spectrum (Fig. S2g) shows doublets at 162.1 eV and 163.3 eV, corresponding to S $2p_{3/2}$ and S $2p_{1/2}$, which are characteristic of metal–sulfide bonds. The presence of a peak at ~168 eV in the S 2p region is typically attributed to surface-adsorbed sulfate species (SO_4^{2-}), resulting from oxidation of sulfide during sample exposure to air.[22] Overall, the XPS data confirm that the as-prepared material is a multi-metal sulfide with the successful incorporation of all constituent elements and slight oxidation.

Transmission electron microscopy (TEM) images (Fig. 1b and c) reveal that the HEMS nanoparticles exhibit a thin nanoflake-like morphology with loosely aggregated features. The high-resolution TEM (HRTEM) image (Fig. 1c) further confirms poorly defined lattice fringes, indicative of an amorphous-like structure, which is consistent with the XRD results. Moreover, the selected-area electron diffraction (SAED) pattern (Fig. 1d) displays diffuse halo rings instead of sharp diffraction spots, further indicating the absence of long-range crystalline order. As shown in Fig. 1e, AFM height analysis of the HEMS flakes reveals a thickness of 1.05 nm, confirming that the synthesized flakes possess uniform and ultrathin morphologies. To provide a structural comparison, XRD (Fig. S3), TEM and energy-dispersive X-ray spectroscopy (EDS) analyses (Fig. S4–S6) were also performed for the ternary sulfide NiCoRuS, which revealed a similar nanoflake morphology and disordered state. Likewise, as shown in Fig. 1f–n, the elements Ni, Co, Fe, Mn, Ru and S are homogeneously dispersed throughout the NiCoFeMnRuS nanoflakes. Furthermore, energy-loss spectroscopy (EELS) analysis confirms the coexistence of Mn, Fe, Co, and Ni within the same nano-region (Fig. S7). Although the Ru M-edge is obscured by the C K-edge from the support film, the EDS spectrum and mapping results validate its incorporation into the HEMS nanoflakes. The actual elemental composition of the synthesized sample was quantitatively determined by inductively coupled plasma optical emission spectrometry (ICP-OES) in Fig. S8. Based on the measured concentrations (mg L^{-1}), the molar amounts of individual elements were calculated and normalized to obtain the atomic fractions. The resulting metal atomic

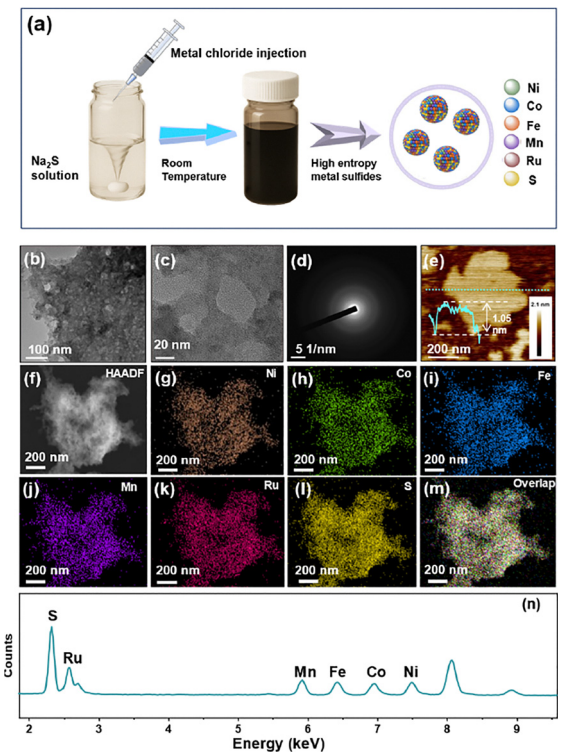

Fig. 1 (a) Schematic illustration of HEMS nanoflake synthesis. (b)–(d) TEM, HRTEM, SAED patterns and (e) AFM images of NiCoFeMnRuS. (f)–(m) EDS mapping images and (n) EDS spectrum of NiCoFeMnRuS.

ratio was determined to be $Ni_{0.228}Co_{0.235}Fe_{0.151}Mn_{0.233}Ru_{0.153}$, indicating a near-equiatomic multicomponent composition. The configurational entropy (ΔS_{config}) was calculated according to the expression:$\Delta S_{config} = -R\sum c_i \ln c_i$, where R is the gas constant and c_i represents the molar fraction of each metal component. The calculated value of approximately 1.59 R exceeds the conventional threshold of 1.5 R, confirming the high-entropy nature of the NiCoFeMnRuS system and substantiating the entropy-stabilized solid-solution formation.

The urea oxidation performance of NiCoFeMnRuS was systematically evaluated and compared with related metal sulfide materials under alkaline conditions. As shown in Fig. 2a, the linear sweep voltammetry (LSV) curves demonstrate that NiCoFeMnRuS exhibits a significantly higher current density in 1 M KOH + 0.5 M urea solution than in either 1 M KOH or 0.5 M urea alone, indicating its pronounced catalytic activity toward the UOR. Fig. 2b compares the overpotentials required to reach current densities of 50, 100, and 200 mA cm^{-2}. The NiCoFeMnRuS catalyst achieves 50 mA cm^{-2} at a low potential of 1.32 V *vs.* RHE, which is markedly lower than that of the OER counterpart (1.51 V) under the same conditions. Even at high current densities (200 mA cm^{-2}), the UOR potential remains favorable (1.38 V), underscoring the HEMS potential for practical applications. The corresponding Tafel plots in Fig. 2c reveal a much smaller Tafel slope for the UOR (46.6 mV dec^{-1}) compared to the OER (76.8 mV dec^{-1}) extracted by linear fitting in the same range (log$j$ = 1.75–2.25), suggesting more favorable reaction kinetics for urea electro-oxidation. To further assess the effect of multi-metal incorporation, Fig. 2d compares the UOR performance of NiCoFeMnRuS with that of NiCoRuS, NiS, and bare Ni foam. Among these, NiCoFeMnRuS shows the lowest potential of 1.33 V at 10 mA cm^{-2} compared with other catalysts. To assess the intrinsic reaction kinetics under kinetic control, Tafel slopes were extracted by linear fitting in the same current-density range (log$j$ = 1.0–1.4) for all catalysts to ensure a meaningful comparison. Tafel analysis in Fig. 2e reveals the superior kinetics of NiCoFeMnRuS, which exhibits a Tafel slope of 30.7 mV dec^{-1}, compared to 64.1 mV dec^{-1} for NiS and 51.1 mV dec^{-1} for NiCoRuS. The Nyquist plots (Fig. 2f) exhibit semicircular profiles whose diameters correspond to the charge-transfer resistance (R_{ct}). The NiCoFeMnRuS electrode displays the smallest semicircle, indicating the lowest R_{ct} and the most favorable charge-transfer kinetics among the compared catalysts. Specifically, the R_{ct} values are 7.41 Ω for NiS, 5.31 Ω for NiCoRuS, and 2.21 Ω for NiCoFeMnRuS, respectively. The substantially reduced R_{ct} of NiCoFeMnRuS indicates more favorable interfacial charge-transfer kinetics, which is consistent with its enhanced urea oxidation activity. Such enhancement can be ascribed to the optimized electronic structure and synergistic interactions among multiple metal sites that facilitate urea oxidation intermediate adsorption. Finally, a long-term chronoamperometry test (Fig. S9) demonstrates excellent stability of the NiCoFeMnRuS catalyst over 120 h of continuous operation at a constant current density of 50 mA cm^{-2} with negligible potential decay, confirming its robust operational durability. To clarify the morphological evolution and structural stability, post-UOR characterizations (Fig. S10–S14) were conducted to reveal a distinct surface reconstruction involving the emergence of nanosheets and sulfur depletion. This confirms the *in situ* formation of an M-OOH active layer, identifying it as the true origin of the superior UOR performance.[23]

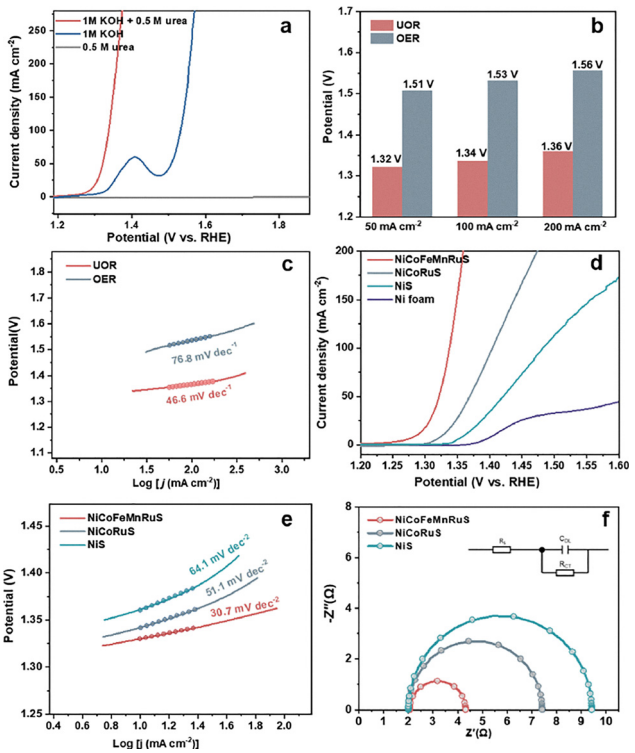

Fig. 2 (a) LSV curves of NiCoFeMnRuS in 1 M KOH + 0.5 M urea, 1 M KOH, and 0.5 M urea solutions. (b) Overpotentials at 50, 100, and 200 mA cm^{-2} for the UOR and OER. (c) Tafel plots for the UOR and OER. (d) Comparison of UOR activity among catalysts. (e) Tafel slopes of different catalysts. (f) Nyquist plots from EIS analysis.

Practical overall urea electrolysis was evaluated using a NiCoFeMnRuS anode and Pt/C cathode (Fig. 3a). This system exploits the lower potential of urea oxidation compared to the OER, enabling simultaneous energy-efficient hydrogen production and direct wastewater remediation. The polarization curves in Fig. 3b clearly demonstrate the energy-saving advantage of urea electrolysis. At the current density of 50 mA cm^{-2}, the system requires only 1.5 V, which is 0.19 V lower than that needed for water splitting under the same conditions. Fig. 3c and Table S1 compare the cell voltages of various recently reported catalysts at a current density of 10 mA cm^{-2}. The NiCoFeMnRuS catalyst exhibits competitive performance, demonstrating a lower operating voltage than most non-precious metal systems. This highlights the enhanced catalytic activity attributed to its high-entropy composition. Finally, Fig. 3d demonstrates the long-term stability of the system, maintaining steady performance over a 20-hour electrochemical durability test. The cell voltage shows only a slight increase during operation, indicating that the NiCoFeMnRuS catalyst retains excellent electrochemical stability.

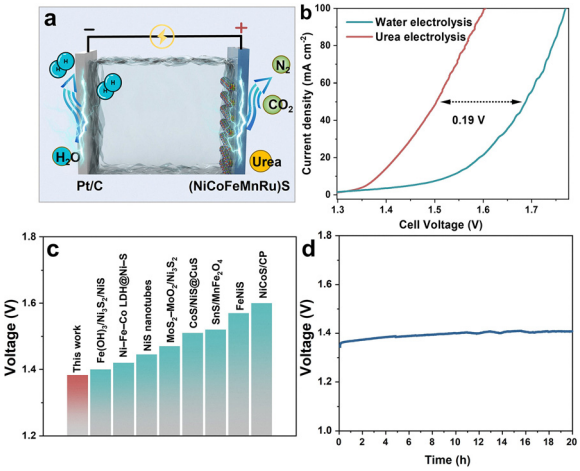

Fig. 3 Overall urea electrolysis performance of the NiCoFeMnRuS catalyst. (a) Schematic of the two-electrode urea electrolyzer system. (b) Polarization curves of urea and water electrolysis. (c) Performance benchmarking of the NiCoFeMnRuS against representative reported catalysts. (d) Long-term galvanostatic stability test.

In conclusion, we report a rapid and room-temperature coprecipitation method for preparing NiCoFeMnRuS high-entropy sulfide nanoflakes that show excellent catalytic behavior for the UOR. The synthesis proceeds under ambient conditions, without requiring high-temperature treatment or complex processing steps, making it a convenient and energy-conscious approach for producing multicomponent metal sulfides. The resulting catalyst delivers strong electrocatalytic performance, reaching 50 mA cm^{-2} at a low potential of 1.32 V *vs.* RHE, and maintains stable operation over long periods. Comprehensive structural and surface characterizations confirm the successful formation of a uniform high-entropy structure with low crystallinity and evenly distributed active sites, which together account for its high activity and durability. This work presents a fast synthesis of high-entropy metal sulfides with superior UOR catalytic performance. By coupling urea remediation with hydrogen generation, this strategy offers a dual-functional pathway integrating environmental protection with renewable energy applications.

This work was supported by the Australian Research Council (ARC) Discovery Project (DP260101246 and DP220101959), the ARC Future Fellowship Scheme (FT210100509) and the Hebrew University of Jerusalem - Zelman Cowen Academic Initiatives (ZCAI) Joint Projects 2021. We also acknowledge the Centre for Microscopy, Characterisation and Analysis (CMCA, UWA) and Dr Martin Saunders for their technical assistance with electron microscopy.

Conflicts of interest

There are no conflicts to declare.

Data availability

All data supporting the findings of this study are available within the paper and/or the supplementary information (SI). Supplementary information: detailed synthesis procedures and additional characterization data. Further information related to this work is available from the authors. See DOI: https://doi.org/10.1039/d5cc06830d.

References

1 Z. Yu, Z. Deng, Y. Li and X. Wang, *Adv. Funct. Mater.*, 2024, **34**, 2403435.
2 L. Quan, H. Jiang, G. Mei, Y. Sun and B. You, *Chem. Rev.*, 2024, **124**, 3694–3812.
3 S. Xu, X. Ruan, M. Ganesan, J. Wu, S. K. Ravi and X. Cui, *Adv. Funct. Mater.*, 2024, **34**, 2313309.
4 H. Tang, Z. Sun, S. Fan, S. Feng, L. Li, L. Fang and C. Wang, *Chem. Eng. J.*, 2024, **491**, 152023.
5 J. Zhu, H. Wu, K. Gui, Z. Li, C. Zhang, J. Wang and J. Niu, *Chem. Commun.*, 2022, **58**, 12503–12506.
6 L. Jiang, Y. Pan, J. Zhang, X. Chen, X. Ye, Z. Li, C. Li and Q. Sun, *J. Colloid Interface Sci.*, 2022, **622**, 192–201.
7 A. S. Rasal, H. M. Chen and W.-Y. Yu, *Nano Energy*, 2024, **121**, 109183.
8 Q. Li, J. Wang, Y. Shi, H. Li, H. Yang, K. Xiang, W. You and J. Liang, *Mater. Horiz.*, 2025, 9952–9965.
9 W. Shi, X. Sun, R. Ding, D. Ying, Y. Huang, Y. Huang, C. Tan, Z. Jia and E. Liu, *Chem. Commun.*, 2020, **56**, 6503–6506.
10 M. J. Theibault, C. R. McCormick, S. Lang, R. E. Schaak and H. D. Abruna, *ACS Nano*, 2023, **17**, 18402–18410.
11 W. Rong, Y. Chen, R. Dang, K. Huang, J. Xia, B. Zhang, J. Liu, H. Meng, Q. Cao and J. Wu, *J. Alloys Compd.*, 2024, **971**, 172786.
12 L. Jiang, B. Duan, S. Lin, F. Jones, Y. Li, Z. Wen and G. Jia, *Nano Energy*, 2026, **148**, 111634.
13 Y. Xu, L. Wang, Z. Shi, N. Su, C. Li, Y. Huang, N. Huang, Y. Deng, H. Li, T. Ma, X. Y. Kong, W. Lin, Y. Zhou and L. Ye, *Energy Environ. Sci.*, 2023, **16**, 1531–1539.
14 Q. Yuan, T. Liu, D. Ma, Y. Liao, W. Wang, H. Meng, Q. You, F. Zeng, M. Xie, H. Huang, C. Liu and X. Liang, *J. Colloid Interface Sci.*, 2025, **684**, 783–791.
15 S. L. Fereja, Z. Zhang, Z. Fang, J. Guo, X. Zhang, K. Liu, Z. Li and W. Chen, *ACS Appl. Mater. Interfaces*, 2022, **14**, 38727–38738.
16 Y. Fu, H. Liu, B. Gao, J. Mu, G. Guan and Z. Feng, *Chem. Eng. J.*, 2025, **511**, 162264.
17 H. Zhao, Q. Zhang, X.-W. Gao, J.-Z. Li, H.-K. Liu and W.-B. Luo, *Mater. Adv.*, 2021, **2**, 3752–3759.
18 X. Chen, L. Jiang, W. Guo, S. Shen, Z. Wang, K. Shao, Z. Wang and C. Li, *ACS Appl. Energy Mater.*, 2025, **8**, 751–758.
19 C. Yang, Z. Wang, Z. Li, Y. Pan, L. Jiang, C. Li, C. Wang and Q. Sun, *ChemSusChem*, 2022, **15**, e202200072.
20 L.-M. Lyu, Y.-C. Chang, H.-J. Li, P.-E. Wang, R.-H. Juang, M.-Y. Lu, C.-S. Li and C.-H. Kuo, *Adv. Sci.*, 2025, **12**, 2411622.
21 L.-L. Shen, X. Dong, W. Wang, H. Yu, P. Wu, J. Wang, Y. Xu, X. Cui, X. Li, G.-R. Zhang and D. Mei, *Adv. Funct. Mater.*, 2024, **34**, 2400964.
22 H. Liu, Z. Liu, F. Wang and L. Feng, *Chem. Eng. J.*, 2020, **397**, 125507.
23 J. Gautam, S.-Y. Lee and S.-J. Park, *Adv. Energy Mater.*, 2025, **15**, 2406047.

